INTERNATIONAL JOURNAL FOR NUMERICAL METHODS IN FLUIDS
Int. J. Numer. Meth. Fluids 2009; **61**:1388–1410
Published online 6 February 2009 in Wiley InterScience (www.interscience.wiley.com). DOI: 10.1002/fld.2003

Numerical modelling of cavitation erosion

Matevž Dular[1,*,†] and Olivier Coutier-Delgosha[2]

[1]*Laboratory for Water and Turbine Machines, University of Ljubljana, Aškerčeva 6, 1000 Ljubljana, Slovenia*
[2]*Laboratoire de Mécanique de Lille/ENSAM Lille, 8 Boulevard Louis XIV, 59046 Lille, France*

SUMMARY

The goal of the work is to investigate the possibility of cavitation erosion prediction using computational fluid dynamics (CFD) tools only. For that purpose, a numerical process based on a coupling between CFD and an erosion model is presented and tested in several configurations of cavitating flow on a two-dimensional hydrofoil. The CFD code, which is based on the homogeneous approach, was previously validated on numerous experiments. In the present work, the predictions of velocity and pressure evolutions in the vicinity of the hydrofoil are compared with experimentally measured data. A close agreement is systematically obtained. The erosion model is based on the physical description of phenomena from cavitation cloud implosion, pressure wave emission and its attenuation, micro-jet formation and finally to the pit formation. The coupling between CFD and the erosion model is based on the use of local pressure, void fraction and velocity values to determine the magnitude of damage at a certain point. The results are compared with the experimentally measured damage on the hydrofoil. In the experiments a thin copper foil applied to the surface of the hydrofoil was used as an erosion sensor. A pit-count method was applied to evaluate the damage. The comparison shows that it is possible to use solely CFD tools to predict time evolution of cavitation erosion, including final extent and magnitude, with a very good accuracy. Copyright © 2009 John Wiley & Sons, Ltd.

Received 16 July 2008; Revised 29 October 2008; Accepted 29 December 2008

KEY WORDS: cavitation; erosion; pit count; piv; computational fluid dynamics; erosion model

1. INTRODUCTION

The cavitation damage is caused by bubble collapses in the vicinity of a solid surface. A wide range of studies related to various aspects of the problem—from bubble dynamics to material testing—have been performed. They all aim at improving the physical understanding of the phenomenon.

*Correspondence to: Matevž Dular, Laboratory for Water and Turbine Machines, University of Ljubljana, Aškerčeva 6, 1000 Ljubljana, Slovenia.
†E-mail: matevz.dular@fs.uni-lj.si, matevz.dular@email.si

Contract/grant sponsor: Slovenia-France Cooperation in Science
Contract/grant sponsor: Technology Program Proteus

However, cavitation erosion is complex, because it involves complicated flow phenomena combined with the reaction of the particular material of which the solid surface is composed.

It is recognized that the most common mechanism of cavitation erosion is the so-called micro-jet phenomenon [1]. Benjamin and Ellis [2] provided experimental proof of micro-jet formation. The process was later theoretically approached by Plesset and Chapman [3] and again experimentally confirmed by Lauterborn and Bolle [4] who provided high-speed photographic observations of the initial stages of the collapse of a laser-generated bubble near the wall. It was found that the liquid jet that penetrates the bubble can reach a velocity of several 100 m/s.

The process of formation of cavitation damage begins with cavitation cloud separation. The cavitation cloud travels with the flow and collapses in a higher pressure region. The shock wave emitted at cavitation cloud collapse reaches a magnitude of up to several MPa and influences the bubbles that are positioned near the wall. The pressure wave with sufficient magnitude, acts on the bubbles of a spherical shape that are positioned close to the surface of the submerged body. The shape of the bubble becomes unstable—it begins to oscillate. If the amplitude of oscillations is big enough, a micro-jet phenomenon can occur. The fluid that surrounds the bubble takes a shape of jet through the bubble in the direction towards the solid surface. This micro-jet can reach high local velocities (several 100 m/s) that cause a shock (the order of magnitude is bigger than 1 GPa, the duration is approximately 1 ns and the affected area is in order of a few μm^2) with high local tension of the material. The damage of the surface appears in a form of microscopic plastic deformations, called pits.

There were many attempts to predict the magnitude of the cavitation erosion. For example, Pereira *et al.* [5] found a relation between the volume of transient cavities and its rate of production to the material deformation energy. Fortes-Patella *et al.* [6] suggested that the damage of the solid surface was due to a sequence of events from cavitation cloud collapse to the spherical implosion of a single bubble that causes the damage. Finally present author Dular *et al.* [7] showed that specific visual information of cavitation can be used to predict cavitation erosion. However, none of the above-mentioned papers describe a complete coupling between computational fluid dynamics (CFD) and an erosion model, which is the case of the present study.

In the present work, a numerical process based on a coupling between CFD and an erosion model is presented and tested in several configurations of cavitating flow on a 2D hydrofoil. For the CFD part of the process, the 'in house' 2D cavitating unsteady code IZ, which belongs to the CNES (French space agency) is used. Unsteady simulations are based on a homogeneous cavitation model, where the density variations are controlled by a barotropic state law that links them directly to the pressure field evolution. The erosion model is derived from the work of Dular *et al.* [8]. It is based on the theories proposed by Plesset and Chapman [3] and Lush [9] to explain micro-jet formation and pit appearance and also on additional measurements performed recently by Dular *et al.* [7, 10]. The coupling consists of a transfer of information from CFD to the erosion model: data obtained by CFD simulation are used at each time step, so that the erosion model calculates the time evolution of cavitation erosion, as well as its final extent and damage magnitude.

Section 2 presents the experimental measurements. Two types of investigations have been performed: (i) measurement of pressure and velocities close to the hydrofoil, for the purpose of CFD validation in the present flow configuration, (ii) measurement of the damage due to cavitation erosion for comparison with the numerical predictions. Section 3 focuses on the erosion model, while the CFD tool and the validation tests are presented in Section 4. In Section 5, the numerical coupling between CFD and an erosion model is described in detail and the cavitation erosion predicted by the numerical approach is compared with the experimental data.

DOI: 10.1002/fld

2. EXPERIMENTAL INVESTIGATIONS

The experiments were performed in a cavitation tunnel at the laboratory for turbomachinery and fluid power (Darmstadt University of Technology, Germany). Experimental techniques are only briefly presented hereafter, while a more extensive discussion of this part of the work can be found in Dular *et al.* [7, 11, 12].

A simple 16 mm thick 50 mm wide and 107.9 mm long symmetric hydrofoil was used for the experiments. It has a circular leading edge and a wedge shape trailing edge. The even 70 mm long surface in the middle of the hydrofoil gives an ideal geometry for conducting erosion measurements (Figure 1).

The hydrofoil was put into a rectangular measuring section of the cavitation tunnel with closed circuit which enabled to vary the system pressure and consequently the cavitation number (Figure 2). The test section of the cavitation tunnel is 500 mm long, 100 mm high and 50 mm wide. Two observation windows are mounted for top and side view observation.

A 5° incidence of the hydrofoil is systematically applied in the present work. A low content of dissolved and undissolved gasses ($14.3\pm0.5\,mg_g/l_w$—milligram of gas per liter of water) is imposed

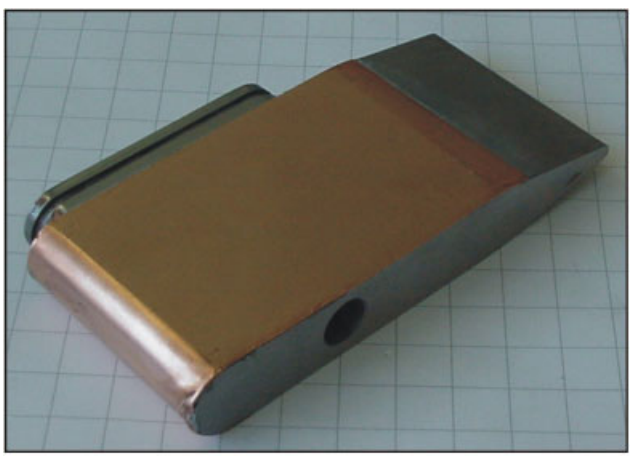

Figure 1. Copper coated hydrofoil.

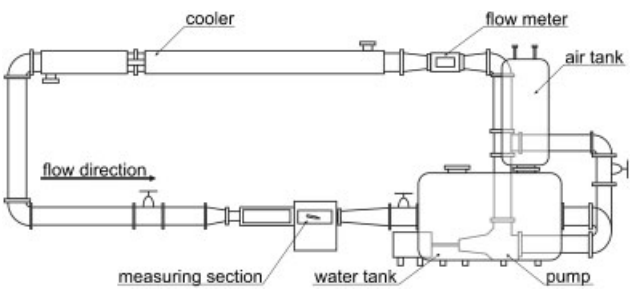

Figure 2. Closed-loop cavitation tunnel.

DOI: 10.1002/fld

by running the facility at a low system pressure (0.2 bar) for about 30 min. The cavitation number σ is based on the pressure at the inlet of the test section p_∞ (measured at the position 400 mm upstream from the hydrofoil) and on the vapor pressure p_v (at system temperature) divided by the dynamic pressure (defined by fluid density ρ and upstream flow velocity v):

$$\sigma = \frac{p_\infty - p_v}{\rho \cdot v^{2/2}} \tag{1}$$

Considering the combination of inaccuracies of pressure, velocity and temperature measurements, the cavitation number was determined with a maximum global uncertainty of ± 0.03. Four cavitation conditions have been investigated.

Developed cavitating flow including periodical vapor shedding was systematically observed.

The experimental work is composed of two parts:

- Measurements of pressure and velocity above the foils surface, for the validation of CFD predictions (Section 4).
- Measurements of the cavitation damage on the hydrofoil surface, for the evaluation of erosion predictions (Section 5).

2.1. Pressure and velocity measurements

Velocity measurements have been conducted in the four flow configurations indicated in Table I. The difficulty of velocimetry in cavitating flow is mainly related to the presence of an interface between the liquid and the vapor structures. If one wants to use particle image velocimetry (PIV) method, the scattering of the laser light at the interface prevents the acquisition of usable images for the PIV analyses. Therefore, the PIV method was combined with laser-induced fluorescence (LIF). This enables to capture the velocity field outside and inside the two-phase flow area.

The region of interest extended over the hydrofoil. Its dimensions are 76 mm in the vertical direction (from the hydrofoil surface) and 90 mm in the min flow direction (from 20 mm upstream of the leading edge to the curvature of the hydrofoil). It was illuminated by a vertical laser light sheet (Nd–YAG-Laser) approximately 1 mm thick and parallel to the flow direction. In order to minimize the wall effects the laser light sheet was positioned in the middle of the hydrofoil span. Special fluorescent tracer particles (polymethylmethacrylate–rhodamin B, diameter 1–20 μm) were added to the water for the PIV measurements. The particles receive light from the laser at a wavelength of 532 nm (green spectrum) and emit light at a wavelength of 590 nm (yellow spectrum). By fitting the charge-coupled device (CCD) camera with an appropriate light filter (that filters the visible light but lets the light in yellow spectrum trough) it is possible to get suitable images of the tracer particles for the PIV analysis. The camera was triggered by the control unit of the PIV-system in combination with the laser shots with a duration of 10 ns. Two images with 30 μs time delay were recorded. The frequency of image capturing was 0.5 Hz. Using the standard

Table I. Parameters of the tested cavitation conditions.

	Cavitation number (dimensionless)	Velocity (m/s)
Test 1	2.0	13
Test 2	2.3	13
Test 3	2.5	13
Test 4	2.3	16

DOI: 10.1002/fld

DANTEC software a cross correlation of the two images of tracer particles was made. The size of the interrogation area was 16×16 pixels and the overlapping was 50%, which resulted in a distance close to 0.65 mm between the vectors. About 35% of vectors were rejected in the area where no flow is present (the part of an image where hydrofoil contour is present). Additionally about 2% of the remaining vectors were recognized as invalid 'bad' vectors and were substituted. The dominant error in the PIV measurements is the bias introduced by the sub-pixel peak finding algorithm, which is in the order of 0.1 pixels, hence the average uncertainty of measured velocity using PIV–LIF technique was estimated to 2%. The technique was extensively discussed in papers by Dular *et al.* [11, 12].

Unsteady pressure measurements were performed on the foil suction side to detect shock waves previously reported by Bohm [13] and Hofmann [14]. Indeed, as the cavitation cloud collapses in the rear part of the hydrofoil, a shock wave is emitted, which then spreads in the two-phase mixture. It is believed that these shockwaves trigger a sequence of events that consequently lead to cavitation erosion. So, it is of great importance to check that CFD is able to detect these shockwaves with correct magnitude, periodicity and length. Therefore, four pressure transducers Kulite XTM-190M (measuring span 0–17 bar with a frequency range up to 125 kHz) were mounted directly into the hydrofoil. Silicone oil was used to fill the cavities from the transducers membrane to the tapings on the surface of the foil. Silicone oil vapor pressure is by a factor 10^6 smaller than vapor pressure of water to avoid vaporization in the cavities due to the expected under pressures. The positions of transducers were 14.6, 26.6, 38.6 and 50.6 mm downstream from the leading edge of the hydrofoil. The uncertainty of dynamic pressure measurements was $\pm 1\%$ (full scale output).

The original purpose of this experiment was neither evaluation of CFD, nor the prediction of erosion, so only one set of results is available, for flow conditions close to test four conditions ($\sigma = 2.7$, $v = 16\,\mathrm{m/s}$). Despite these slight differences between the present flow conditions and test 4, qualitative comparisons between CFD results and the experiments enable evaluation of capability of the numerical model to predict the amplitude, duration and periodicity of the pressure waves above the foil section.

The comparison between the experimental measurements and the results of CFD are detailed in Section 4.

2.2. Experimental measurement of cavitation erosion

Owing to the time limitation of the experiment, only damage in the incubation period was studied (where damage is already present but there is no material loss).

To get the information about the erosion on the whole surface of the hydrofoil, a polished 0.2 mm thick copper foil was fixed to its surface using an adhesive film (Figure 1). The hardness of the copper coating was approximately 40 HV. For all the cases, the hydrofoil was exposed to cavitation for a period of 1 h during which a sufficient number of pits was obtained.

The order of magnitude of the pits diameter is 10^{-5} m, so pits can be distinguished only by sufficient magnification. Magnified images (50:1) of the pitted surface were acquired using an Olympus BX-40 microscope and a CCD camera. Figure 3 shows an individual image of the surface before and after the exposure to cavitation.

Intensity of cavitation erosion was determined with the pit-count method proposed by Dular *et al.* [7]. The method is based on the assumption that the area of the pitted surface and the number of pits that are created by bubble implosions (micro-jet impacts) in a certain time of exposure to cavitating flow give a quantitative indication of the intensity of cavitation erosion. So, the pit-count

DOI: 10.1002/fld

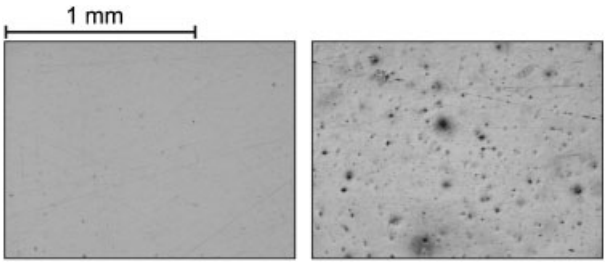

Figure 3. Surface before and after the exposure to cavitation.

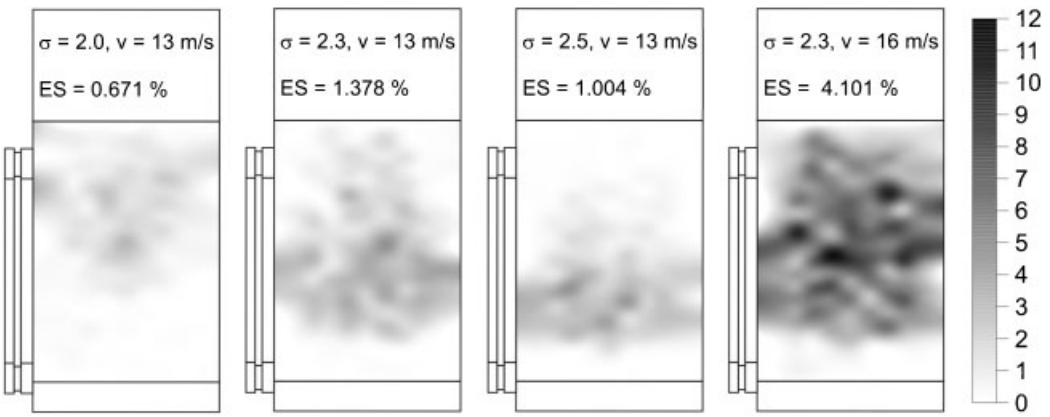

Figure 4. Results of damage evaluation.

method gives a distribution of the number and the area of the pits and consequently the distribution of the magnitude of cavitation erosion on the surface.

One drawback of such a method for the damage evaluation is the possible overlapping of the pits. Pit clusters are created by chance during longer tests, by collapse of a group of bubbles or by rebounds of a single bubble. A test was made and it was concluded that the overlapping of pits would have a significant effect only if the damaged area would cover more than 14% of the whole surface. Although so high pitting rate was not expected this problem was considered. The principle that is used for pit separation is that a single pit cannot form a concave shape. Hence a concavely shaped dark region is divided into a number of individual objects each having a convex shape. The separated objects are then enlarged to fill out the original object size [7].

For each flow condition, 450 1.2×1.5 mm big images of the damages surface were taken. Nine rows of images at distances of 5, 10, 15, 20, 25, 30, 35, 40, 45 mm from the front channel wall were taken; each two images in a row overlapped for about 5–10%. After evaluation by a pit-count method where the damaged area was calculated, a space interpolation was performed to acquire the damage distribution over the whole surface of the hydrofoil. Figure 4 shows the results of the damage measurements. The flow is from bottom to top. The results of surface damage are scaled from 0% surface damage (white) to 12% surface damage (black). The value of eroded surface (ES) represents the part of the whole surface that is damaged (covered by pits).

DOI: 10.1002/fld

Figure 4 shows the results for tests 1–4. For a constant flow velocity of 13 m/s (tests 1–3), it can be observed that the region of maximum cavitation damage moves towards the leading edge when the cavitation number is increased. This was, of course, anticipated since the cavitation extent also decreases in this manner. It can be noticed that the maximum value of total damaged surface (ES) occurs at cavitation number $\sigma = 2.3$, instead of $\sigma = 2.0$ as expected. This result is related to the fact that for $\sigma = 2.0$, the region of cloud implosion lies downstream from the copper-coated surface and also further away from the hydrofoil surface than in the other cases.

Test 4 with higher flow velocity (16 m/s) revealed an expected relation between flow velocity and an erosion rate. The cavitation is much more aggressive at higher flow velocities. The distribution of the pits and the position of the maximum magnitude of damage are similar to test 2, which is performed at the same cavitation number but with lower velocity. Indeed, topology of cavitation does not change significantly with velocity. It was also shown by Dular *et al.* [10] where an additional experiment at flow velocity of $v = 10$ m/s was made that the relationship of aggressiveness versus flow velocity obeys a very well-known power law with an exponent of 6.1.

3. EROSION MODEL

A successful prediction of the erosion process is a major issue to obtain satisfactory numerical predictions of the cavitation damage. The process of pit formation is very complex. The presented theory explains the pit formation in the following way:

1. Collapse of the cavitation cloud causes a shock wave that spreads in the fluid.
2. The magnitude of the shock wave is attenuated as it travels towards the solid surface.
3. Single bubbles are present near the solid surface. As the shock wave reaches them, they begin to oscillate and a micro-jet phenomenon can occur.
4. The damage (single pit) is caused by high-velocity liquid jet impact on the solid surface.

If only the incubation period (where the surface is plastically deformed without any material loss) is considered, it can be stated that the ES of a submerged body results from repetition of the above-mentioned process.

Items 1 and 2, i.e. prediction of the pressure peaks on the solid surface that result from cloud collapses, are obtained by the CFD calculations presented hereafter in Section 4, while items 3 and 4 are managed by the erosion model detailed in the present section. Of course, several other issues arose during the model development and had to be additionally addressed.

3.1. Formation of micro-jet

The presence of a solid surface can influence the bubble collapse process so that it becomes asymmetrical. A well-known theory developed by Plesset and Chapman [3] determines the jet velocity, which is:

$$v_{\text{jet}} = 8.97\gamma^2 \sqrt{\frac{p - p_v}{\rho}} \tag{2}$$

where γ is the non-dimensional distance from the bubble center to the surface ($\gamma = H/R$, where H is the distance and R is the bubble radius).

DOI: 10.1002/fld

3.2. Pit formation

The water hammer stress applied to the material at the impact of the liquid micro-jet can be considered as the main mechanism responsible for the damage of the solid surface [3]. If the density and the sonic velocity of the solid are high compared with the ones of the liquid, it is defined as

$$p \approx v_{\text{jet}} \rho_{\text{l}} c_{\text{l}} \tag{3}$$

where ρ_{l} and c_{l} are the density and the sonic velocity in the pure liquid, respectively.

In the present approach, the surface responds as a perfectly rigid solid until a certain compressive stress is reached and then behaves as a perfectly plastic solid, for which the stress will remain constant. The deformation only occurs if the water hammer pressure is higher than the limit pressure at which the plastic flow of the material occurs. This condition results in a critical velocity for which the yield stress p_{y} of the material (high enough to produce a plastic flow) is reached. Its expression was derived by Lush [9] and reads:

$$v_{\text{crit}} = \sqrt{\frac{p_{\text{y}}}{\rho_{\text{l}}} \left(1 - \left(1 + \frac{p_{\text{y}}}{B}\right)^{-1/n}\right)} \tag{4}$$

where p_{y} denotes the yield stress of the material, $B = 300\,\text{MPa}$ and $n = 7$.

A part of the water hammer pressure wave equation (3) energy is needed to reach the plastic flow condition of the material. The other part p_{def} of the pressure is converted into deformation energy

$$p_{\text{def}} \approx v_{\text{def}} \rho_{\text{l}} c_{\text{l}} = (v_{\text{jet}} - v_{\text{crit}}) \rho_{\text{l}} c_{\text{l}} \tag{5}$$

where p_{def} and v_{def} denote the deformation pressure and the deformation velocity, respectively.

The duration of the water hammer stress corresponds to the time needed for the impact signal to cross the radius of the jet r_{jet}:

$$t_{\text{def}} = \frac{r_{\text{jet}}}{c_{\text{l}}} \tag{6}$$

After that time a stagnation pressure $\frac{1}{2}\rho v^2$ is established. It is unlikely that any damage occurs in this period since the stagnation pressure is an order of magnitude smaller than the water hammer pressure (unless exceptionally high impact velocities are encountered).

If we consider only the center of the impact where motion (plastic flow) normal to the surface is present, then the maximum depth of the pit can be calculated:

$$d_{\text{pit}} = v_{\text{def}} t_{\text{def}} \tag{7}$$

The ratio between the pit radius and pit depth is not constant. Previous investigations showed that it usually lies between 15 and 30, but it can also be as low as 2 and as high as 500 [15]. The mean ratio between the pit radius and pit depth (26.7) was determined from laser profilometry measurements of the pitted surface of a copper specimen from the hydrofoil obtained in the same cavitation tunnel done at LEGI–Grenoble [16]. Hence the pit radius is defined as:

$$r_{\text{pit}} = 26.7 d_{\text{pit}} \tag{8}$$

The area of the pit seen normal to the material surface can thus be expressed as:

$$A_{\text{pit}} = \pi \cdot r_{\text{pit}}^2 \tag{9}$$

DOI: 10.1002/fld

3.3. Extrapolation in time

It was recently shown by Dular and Osterman [17] that the cavitation damage in average progresses at a linear rate during the incubation period. It means that only a short period t has to be simulated (several periods of cavitation cloud shedding) to determine the initial damage rate. After that the sustained damage (the part of the damaged surface after a longer amount of time τ) caused by cavitating flow within the incubation period can simply be written as

$$A_{\mathrm{dam}} = \frac{\sum_{t=0}^{t} A_{\mathrm{pit}}}{A_{\mathrm{ref}}} \cdot \frac{\tau}{t} \tag{10}$$

where the sum of the pits areas refers to the pits accumulated within the time of the simulation and A_{ref} is the reference area, which is in our case defined by the size of the mesh near the hydrofoil wall. As already mentioned, Equation (10) is only valid during the incubation period of cavitation erosion where no mass loss is present.

4. CFD SIMULATIONS

4.1. Physical model of cavitation

The numerical simulations of the two-phase flow are based on a single fluid model: the liquid/vapor mixture is considered as a homogeneous medium whose density ρ varies in the computational domain according to a barotropic state law (Figure 5).

According to this law, when the local pressure in a cell is higher than the neighborhood of the vapor pressure $P_v (P > P_v + (\Delta P_v/2))$, the fluid is supposed to be purely liquid. It means that the

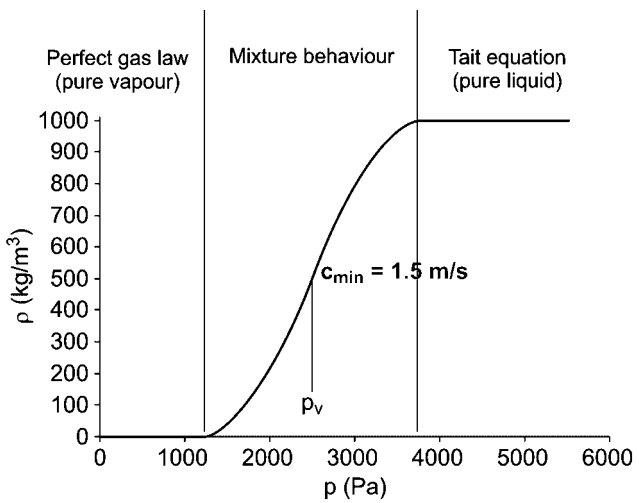

Figure 5. Barotropic state law.

DOI: 10.1002/fld

entire cell is occupied by liquid and the local density ρ is calculated by the Tait equation [18]

$$\frac{\rho}{\rho_{\text{ref}}} = \sqrt[n]{\frac{p+B}{p_{\text{ref}}+B}} \tag{11}$$

where $p_{\text{ref}} = P_{\text{outlet}}$ and $\rho_{\text{ref}} = \rho_{l\,\text{outlet}}$ are reference pressure and density considered at the outlet of the computational domain and for water $B = 300\,\text{MPa}$, $n = 7$.

If the pressure is lower than the neighborhood of the vapor pressure ($p < p_v - (\Delta p_v/2)$), the cell is full of vapor and the local density ρ is given by the perfect gas law. Between purely vapor and liquid states, the cell is occupied by a liquid/vapor mixture, which is considered as one single fluid with a variable density ρ. This one is directly related to the void fraction $\alpha = (\rho - \rho_l)/(\rho_v - \rho_l)$ corresponding to the local ratio of vapor contained in this mixture.

In direct relation with the range Δp_v, the law is characterized mainly by its maximum slope $1/C_{\text{min}}^2$, where $C_{\text{min}}^2 = \partial P/\partial\rho$. C_{min} can thus be interpreted as the minimum speed of sound in the mixture. Its calibration was done in previous studies [19, 20]. The optimal value was found to be independent of the hydrodynamic conditions and is about 1.5 m/s for cold water.

4.2. Numerical resolution

The simulations are based on 2D calculations of the flow. The mass and momentum equations are solved in the orthogonal frame of curvilinear coordinates (ξ, η), which leads to the following system of four equations:

$$\begin{gathered} S\frac{\partial}{\partial t}(\rho\Phi) + \nabla_\xi\left(\rho u\Phi - \Gamma_\Phi\frac{\partial\Phi}{\partial\xi}\right) + \nabla\eta\left(\rho v\Phi - \Gamma_\Phi\frac{\partial\Phi}{\partial\eta}\right) = S_\Phi \\ \rho = F(Cp, \sigma) \end{gathered} \tag{12}$$

where Φ stands either for 1, u, or v, Γ_Φ is the diffusion coefficient, u and v are the velocity components along coordinates ξ and η, respectively, ∇_ξ and ∇_η are the physical components of the divergence operator along the curvilinear coordinates, S_Φ is the source term, Cp is the non-dimensional pressure coefficient and σ is the cavitation number. The energy equation is not solved, since thermal effects are presently neglected.

A finite volume discretization of these equations is used: the diffusive terms are calculated in a purely central manner, while the convection terms are calculated with the non-oscillatory second-order hybrid linear/parabolic approximation scheme proposed by Zhu [21]. This is a second-order scheme, which locally switches to first order, to prevent numerical oscillations in critical high pressure or high density gradient areas. The time integration is performed with a second-order implicit scheme:

$$\frac{\partial(\rho\Phi)}{\partial t} = \frac{1.5\rho^{n+1}\Phi^{n+1} - 2\rho^n\Phi^n + 0.5\rho^{n-1}\Phi^{n-1}}{\Delta t} \tag{13}$$

The basis of the numerical resolution is the SIMPLE algorithm proposed by Patankar [22] for incompressible flow. Each physical time step is composed of successive iterations, which march the solution towards convergence. The initial scheme has been modified to treat as well the nearly

DOI: 10.1002/fld

incompressible parts of the flow as the highly compressible ones in the liquid/vapor mixture [20]. The main steps of a single iteration are listed hereafter.

- Resolution of the transport equations for the turbulent variables and calculation of the turbulent viscosity ν_t.
- Calculation of the estimated velocities $\mathbf{U}^*(u^*, v^*)$ from the momentum balance equations.
- Calculation of the density ρ^* and its derivative $(\partial\rho/\partial P)$, according to the barotropic state law.
- Resolution of the pressure correction equation. It is derived from the mass balance equation, which is discretized in each cell according to the following expression:

$$1.5\frac{S}{\Delta t}\rho_p^{n+1} = -\rho_e^{n+1}u_e^{n+1}\Delta\xi_e + \rho_w^{n+1}u_w^{n+1}\Delta\xi_w - \rho_n^{n+1}v_n^{n+1}\Delta\eta_n + \rho_s^{n+1}v_s^{n+1}\Delta\eta_s + S_\rho^n \quad (14)$$

  where S is the cell area, 'P' denotes the current cell, and 'e', 'w', 'n','s' denote the east, west, north, and south neighboring cells. S_ρ^n contains the explicit source terms resulting from the time discretization.

To obtain the final pressure correction equation, velocities u and v are replaced by $u^* + \mathrm{d}u$, $v^* + \mathrm{d}v$, respectively, while ρ is replaced by $\rho^* + \mathrm{d}\rho$. Thus, the expression of the pressure correction equation yields not only velocity variations $\mathbf{dU}(\mathrm{d}u, \mathrm{d}v)$, but also supplementary terms involving variations $\mathrm{d}\rho$. The term $\mathbf{dU}$ is derived from a simplified differential form of the momentum balance equation, while $\mathrm{d}\rho$ is written as follows:

$$\mathrm{d}\rho_{i,j} = \left(\frac{\partial\rho}{\partial P}\right)_{i,j}\mathrm{d}P_{i,j} \quad (15)$$

- when the pressure correction $\mathrm{d}P$ is obtained, not only the velocity and the pressure, but also the density values are corrected, according to the following expression:

$$\rho = \rho^* + \left(\frac{\partial\rho}{\partial P}\right)\mathrm{d}P \quad (16)$$

Densities obtained from Equation (16) may be outside from the physical range [0, 1], because of the high local values of $\partial\rho/\partial P$ in the two-phase mixture. Non-physical values are thus corrected and a supplementary loop over the pressure correction step is performed until all values of the void ratio are obtained inside their physical range [0, 1].

4.3. Turbulence model

Most of the simulations of cloud cavitation in turbulent flow require a special attention to the model of turbulence to be paid [19, 20, 23]. Indeed, using a standard two-equation turbulence model leads to a complete stabilization of the flow, while in experiments a periodical self-oscillation behavior involving large vapor cloud shedding is observed. This discrepancy is mainly due to the over-estimation of the turbulent dissipation in the cavity downstream end, which stops prematurely the re-entrant jet and thus inhibits the flow unsteadiness. In the case of the present physical cavitation model, Coutier-Delgosha *et al.* [23] have suggested that taking into account the effects of the mixture compressibility in the turbulence model may be necessary to obtain the correct periodical behavior of the cavity. A simple correction of the k–ε RNG (renormalization group) model, initially

DOI: 10.1002/fld

proposed by Reboud *et al.* [19], was shown to enable a substantial improvement of the simulations. This correction can be applied directly in the expression of the turbulent viscosity by writing it $\mu_t = f(\rho) C_\mu k^2/\varepsilon$ instead of $\mu_t = C_\mu k^2/\varepsilon$ for a single-phase flow. The function $f(\rho)$ is expressed as follows:

$$f(\rho) = \rho_v + (1-\alpha)^n (\rho_l - \rho_v) \tag{17}$$

with $n = 10$.

The function f is then equal to ρ_v or ρ_1 in the regions containing, respectively, pure vapor or pure liquid, but it decreases rapidly towards ρ_v for intermediate void ratios. This modification was applied previously in several configurations (Venturi-type sections, foil sections, cascade of hydrofoils) and the results of the simulations were found in fair agreement with the unsteady flow properties obtained in experiments [24]. A similar improvement was achieved by using the corrections proposed by Wilcox [25] in his k–ω model to model compressible fluids.

The modified k–ε RNG turbulence model is applied in the computations presented hereafter. All parameters of the model, excepted the function $f(\rho)$, are set to the value proposed by Orszag [26].

4.4. Grid, boundary and initial conditions

Imposed inlet velocity and fixed outlet pressure boundary conditions are applied. Standard wall functions are used along solid boundaries, so the first grid points are located at a non-dimensional distance from the walls y^+ varying between 30 and 50.

The numerical process to obtain cavitating conditions is based on the experimental procedure. A first stationary time step is first computed with a high-pressure level at the domain outlet to avoid any flow vaporization. Then, the outlet pressure is decreased slowly during the first hundred time steps, from initial non-cavitating conditions down to reach the desired value of the cavitation number σ. Liquid passing on the foil suction side progressively vaporizes during this decrease. After that the outlet pressure is kept constant and the calculation is continued during 100 T_{ref}, where $T_{\text{ref}} = L_{\text{ref}}/V_{\text{ref}}$ with $L_{\text{ref}} = 0.1079\,\text{m}$ the chord length and $V_{\text{ref}} = 13$ or $16\,\text{m/s}$ the inlet flow velocity. So T_{ref} is representative for the transit time of the flow over the foil section. The time step Δt equals $T_{\text{ref}}/200$: this value is derived from the study performed by Coutier-Delgosha *et al.* [23] concerning the influence of the numerical parameters on the simulation of cloud cavitation in a Venturi-type section. One hundred T_{ref} of calculation represent about 0.5–0.8 s, which is sufficient in the present case to characterize the cavitating flow (oscillation frequency, mean and maximal cavitation length, pressure waves, etc.).

To focus on cavitation erosion on the foil surface, the pressure waves resulting from the cavitation collapse on the foil suction side has to be correctly simulated by the numerical model. The intensity and characteristic time of this pressure wave have especially to be correctly predicted. For that purpose, the calculations were continued during 5 T_{ref} with a smaller time step $\Delta t = T_{\text{ref}}/1000$.

The geometry of the computational domain corresponds to the geometry of the experimental test section and the foil position in the test section (Figure 6).

A 630×50 C-type orthogonal mesh was used. The C-type was chosen because of the foil rounded leading edge: using H-type mesh would automatically lead to a locally distorted grid, which is incompatible with the curvilinear orthogonal coordinates. Most of the cells are located around the foil and a contraction of the grid is applied in its upstream part, to obtain an especially fine discretization of the areas where cavitation is expected (Figure 7).

DOI: 10.1002/fld

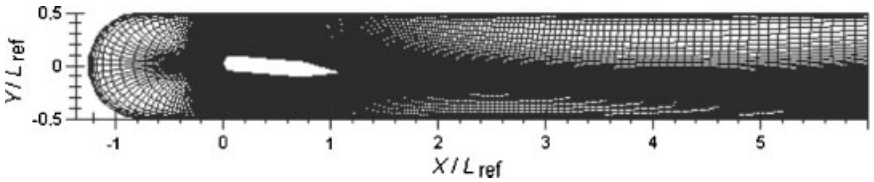

Figure 6. Computational domain.

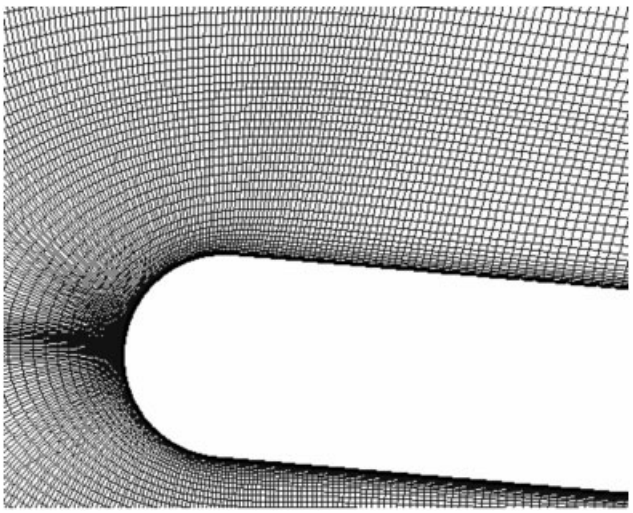

Figure 7. Mesh close to the leading edge.

In the present case the grid size is consistent with the recommendations reported in paper by Coutier-Delgosha *et al.* [23] where the influence of the mesh resolution on the simulation of cloud cavitation was studied.

4.5. Validations of the simulations

The numerical model used for the present simulation was already extensively evaluated [20, 23], hence only a brief comparison of measured and predicted velocity fields and pressure dynamics is presented here.

Sequence of images recorded with a camera and predicted by numerical simulations is presented in Figure 8. The cavitation number is $\sigma = 2.0$ and the reference velocity $v = 13\,\mathrm{m/s}$ (test 1). The length of the sequence is close to 3 ms. It can be seen that the cavitation structure first grows after that the re-entrant jet (not seen in the sequence) causes the cavitation cloud separation. The separated cloud travels with the flow and implodes downstream in a higher pressure region. The implosion of the cloud forms a new re-entrant jet that causes the next cavitation cloud separation. This global unsteady behavior is well predicted by the model.

DOI: 10.1002/fld

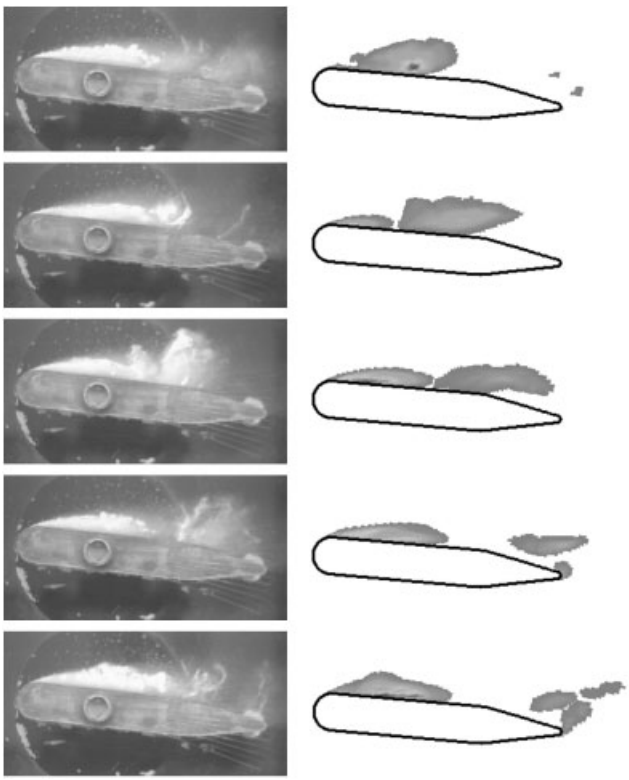

Figure 8. Recorded and simulated cavitation cloud separation.

A comparison between the time-averaged experimental and numerical velocity profiles is presented in Figures 9 and 10 for flow conditions of test 1. Experimental data are obtained from PIV experiments, while numerical data are calculated by time averaging the results recorded between $t/T_{\text{ref}} = 10$ and 100 (end of simulaton) to avoid the effects of the initial transient.

Component u of the velocity (horizontal direction) is first investigated (Figure 9), at five stations above the hydrofoil. As mentioned previously, the measuring plane in the experiments was positioned at half-span of the hydrofoil, so the wall effects are minimized, which is favorable for comparison with the present 2D simulations. The bold horizontal lines in the diagrams represent the position of the hydrofoil surface. A general correct agreement is obtained between the simulations and the experiments. Outside from the sheet cavity, the velocity evolution is very well predicted by the model. As we move towards the surface, the flow velocity starts to decrease (the transition generally occurs approximately at the boundary of the sheet cavity). For position $x = 0$ mm (leading edge) and $x = 64$ mm (downstream from the sheet cavity), no reverse flow is detected. On the other side at stations $x = 16, 32$, and 48 mm, a re-entrant jet is clearly observed both in numerical and experimental results. The magnitude and extension of the re-entrant jet are correctly predicted by the model, while its thickness is slightly overestimated (see planes $x = 16$ and 32 mm).

DOI: 10.1002/fld

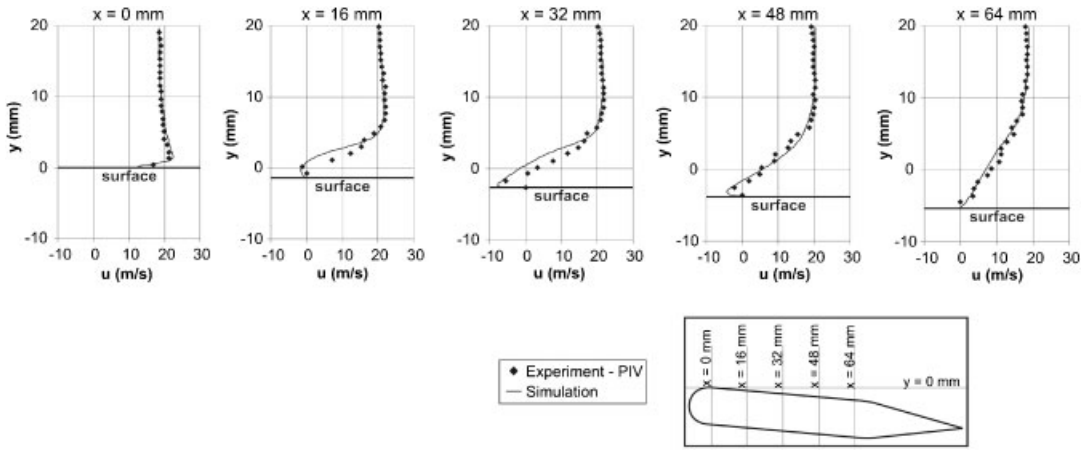

Figure 9. Measured and predicted velocities in the x direction.

Figure 10 focuses on component v of the flow (vertical direction). Predicted and measured velocities on four planes above the hydrofoil are drawn. A good agreement is systematically obtained. A significant increase of velocity component v can be seen close to the hydrofoil leading edge. The effect is more obvious in the vicinity of the hydrofoil (plane $y=0$ mm). The maximal value of v is reached approximately at the point of transition from the circular leading edge to the plane surface of the hydrofoil ($x=20$ mm).

The simulation and experimental measurements also agree well concerning the significant decrease of v downstream from the foil leading edge. Rapid decrease close to the foil surface ($y=0$ mm) and more gradual decrease further away from the hydrofoil surface ($y=5, 10$ and $y=15$ mm) are both correctly predicted by the model. Note that component v approaches a slightly negative value in the rear part of the hydrofoil, because of the incidence angle of 5°.

Figure 11 shows experimentally measured and numerically predicted pressure oscillations at four positions on the hydrofoil surface. Pressure oscillation measurements data were available only for flow condition $\sigma=2.7$ and $v=16$ m/s, for which no erosion measurements were performed. Hence they are compared with the numerical predictions performed at slightly different conditions of test 4 ($\sigma=2.3$, $v=16$ m/s)—we believe that, since the purpose of this comparison is predominately qualitative (only to show that the simulation is capable of prediction of pressure waves), such a comparison is justifiable.

Experimental results (diagrams on the left side) exhibit slight pressure oscillations in time at the first pressure tap. This may be related to the fact that the tap was covered by the sheet cavity during the whole time of experiment. Pressure oscillations are larger at positions p_2 and p_3, where cavitation cloud separations and collapses take place. Magnitude of the pressure peaks can increase up to 14 bar during a short period of time. Such a high pressure cannot cause the erosion by itself but it may carry enough energy to trigger other events, such as micro-jet formation that can be harmful to the material. Chart obtained for tap p_4 shows that the magnitude of the pressure oscillations decreases, which was expected since the last tap lies downstream from the cavitation area.

Numerically predicted evolutions of pressure (right diagrams) are sharper than the measured ones. Moreover, amplitude of the oscillations at tap 1 is much larger. This is related to the fact that the shedding of the vapor cloud is predicted close to the leading edge in the simulations,

DOI: 10.1002/fld

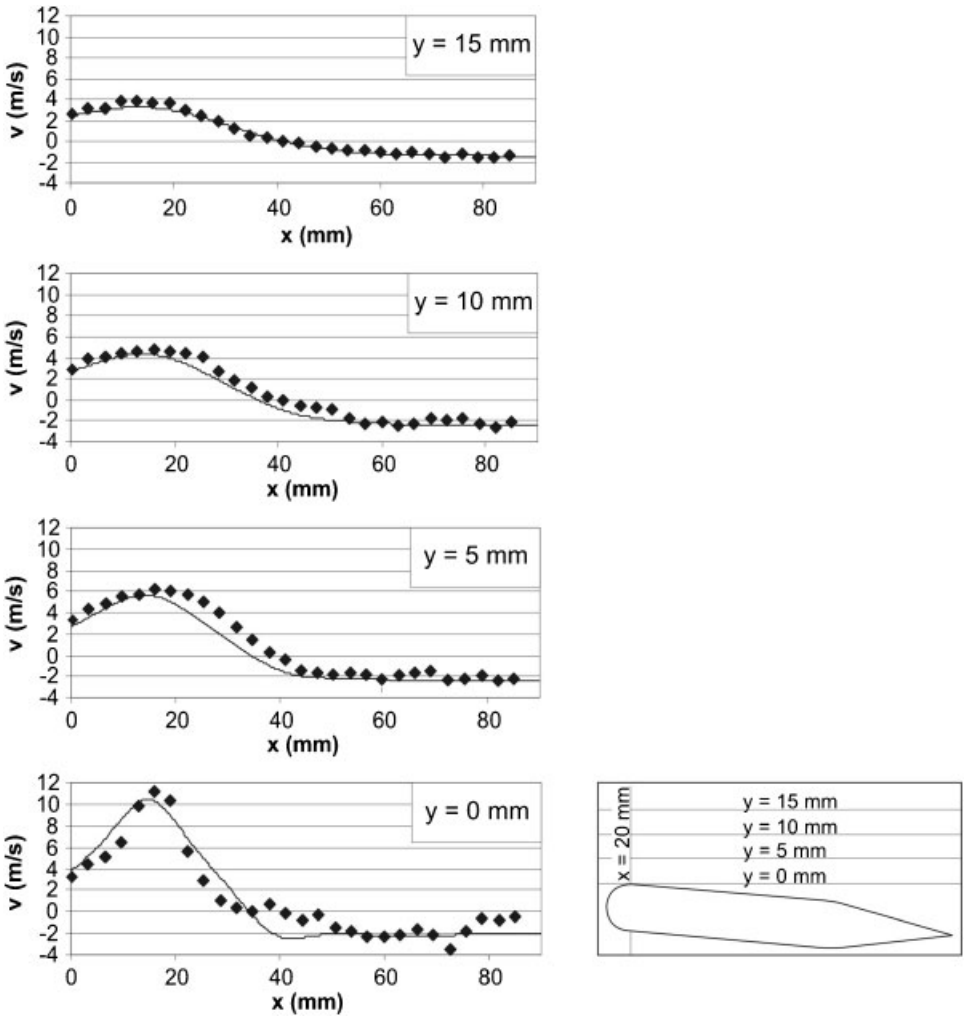

Figure 10. Measured and predicted velocities in the y direction.

whereas it is observed at mid-length of the sheet cavity in the experiments. The oscillations at other positions mimic the real situation with better accuracy. Also the length and the amplitude of the pressure waves are very well predicted.

Frequency of the oscillations results in a predicted value of Strouhal number $St=0.38$ for the cloud shedding ($\sigma=2.3$, $v=16\,\mathrm{m/s}$), which is close to $St=0.42$ obtained in the experiments ($\sigma=2.7$, $v=16\,\mathrm{m/s}$)—and still one has to bear in mind that the results cannot be directly compared (the St number was calculated on the basis of the maximum attached cavity length and the upstream velocity).

These various comparisons enable to assess that the present simulation is capable to predict many aspects of unsteady cavitating flow including the emission of pressure waves, which is indirectly responsible for cavitation erosion.

DOI: 10.1002/fld

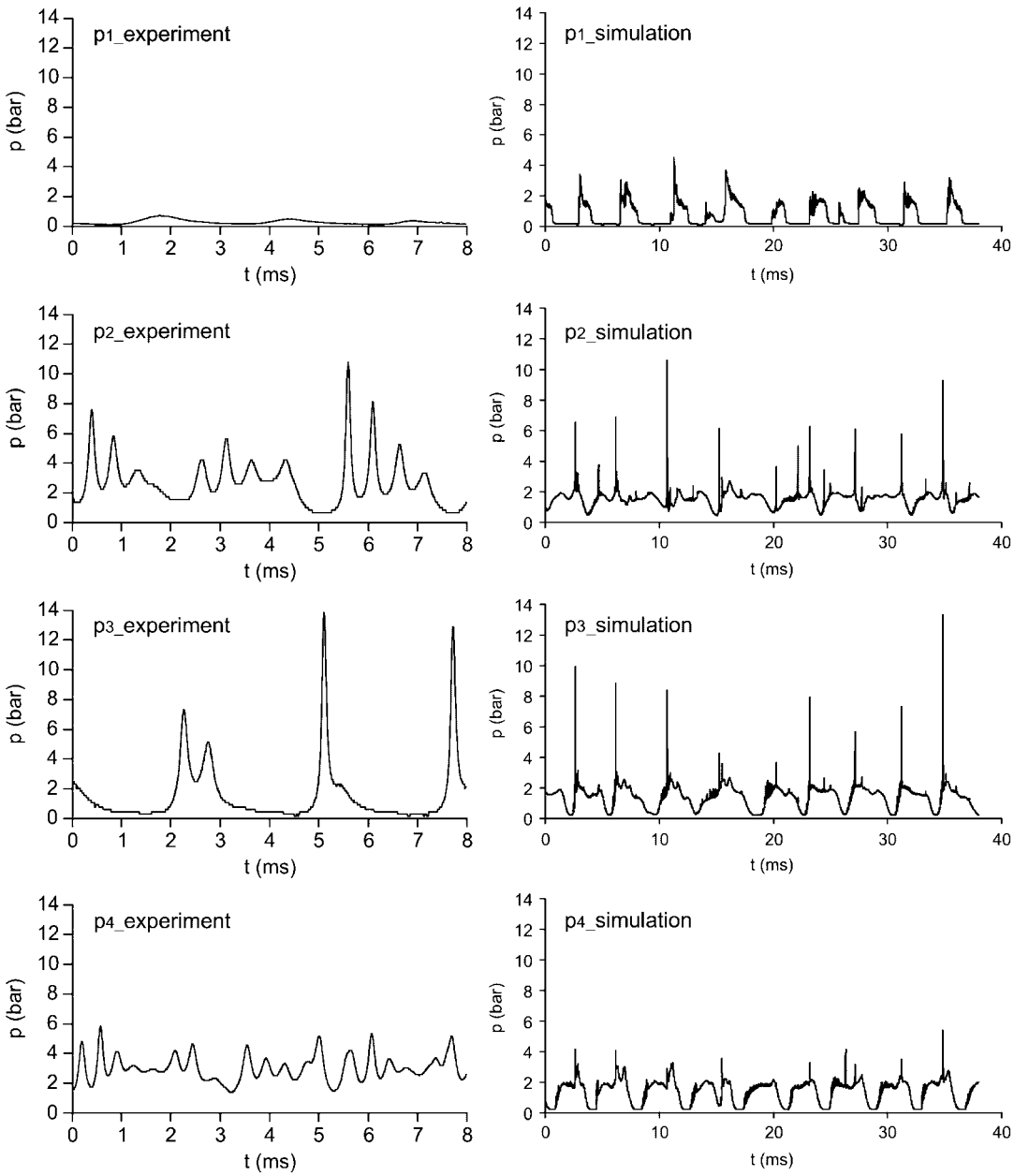

Figure 11. Measured and predicted pressure oscillations.

DOI: 10.1002/fld

5. PREDICTION OF CAVITATION EROSION

5.1. Numerical process

The numerical process for the prediction of cavitation erosion is presented in Figure 12.

At each time step, the solution algorithm solves the governing equations sequentially. Because the governing equations are non-linear and coupled, several iterations of the solution loop must be performed before a converged solution is obtained. The successive steps for a single iteration are outlined below.

1. Fluid properties are updated, based on the current solution. If the calculation has just begun, the fluid properties are updated based on the initialized solution.
2. The momentum equations are each solved in turn using current values for pressure and face mass fluxes, in order to update the velocity field.

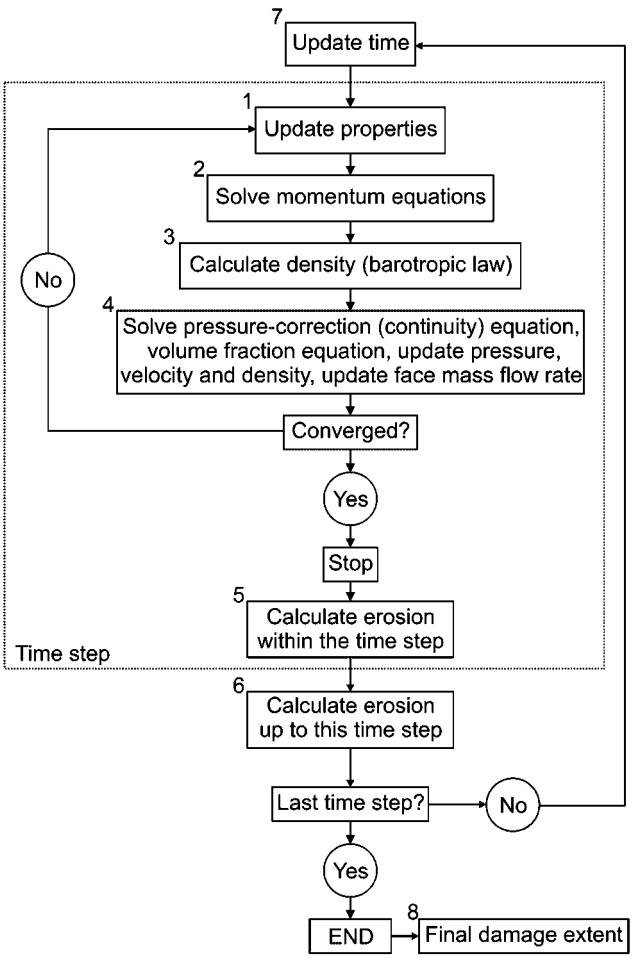

Figure 12. Scheme of the algorithm.

DOI: 10.1002/fld

3. The density and the speed of sound are calculated according to the barotropic state law.
4. Since the velocities obtained in the second step may not satisfy the continuity equation locally, an equation for the pressure correction is derived from the continuity equation and from the linearized momentum equations. This pressure correction equation is then solved to obtain the necessary corrections for the pressure, velocity and density fields and the face mass fluxes, so that continuity is satisfied.

A check for convergence of the equation set is made. If the convergence criteria are not met steps 1–4 are continued until convergence is obtained. If convergence is obtained, calculation continues with item 5.

5. New damage of the surface within the time step is calculated.
6. The new damage is added to the sum of the damage from the previous time steps.
7. The time is updated and the iteration procedure for the new time step begins.

These steps are continued until the last time step is reached.

8. Finally, the desired time of exposure to the cavitation is given and the damage extent is determined through extrapolation.

5.2. *Model parameters*

Besides the straightforward definition of material properties (water and copper coating) two, not easy to determine, values had to be included in the model.

Considering the work by Plesset and Chapman [3], experimental results of Lauterborn and Bolle [4] and in addition by observing the damaged surface, a value of $r_{\text{jet}} = 10\,\mu\text{m}$ was chosen as the most probable value for the average radius of the micro-jet.

On the basis of the same studies, a value of $\gamma = 1.1$ for the non-dimensional distance of the bubble from the solid surface in Equation (2) was chosen.

The values that we have chosen for the present study also proved to work well and produced sensible results in previous studies by the same authors [8].

The values of densities of water and water vapor and the sonic velocity in water correspond to the ambient temperature of 20°C—they are $\rho_{\text{l}} = 998.2\,\text{kg/m}^3$, $\rho_v = 0.5542\,\text{kg/m}^3$ and $c_l = 1484\,\text{m/s}$. The yield stress of the foil made of pure copper (99.9%) is $p_{\text{y}} = 200\,\text{MPa}$.

5.3. *Results*

Owing to the complexity of the problem, the simulated time lasted only 38 ms, but within this period already about 10 cavitation cloud collapses occurred, which is enough for the results to be statistically averaged. Figure 13 shows the evolution of damage accumulation within the short time of simulation. Since the cases do not vary significantly only the results for $\sigma = 2.3$ at $v = 13\,\text{m/s}$ are shown.

We can see that the damage does not progress linearly with time. It can also occur that during one period almost no damage is accumulated in the region where one would expect the highest damage rate—for example between $t = 15.2$ and 22.8 ms. This is of course a result of unsteady and not perfectly periodic nature of cavitation cloud shedding. Also interactions between the pressure waves and the cavity structures can attenuate the effect of cavitation erosion. Although the pit accumulation rate within the short time frame seems to be almost random we are confident that

DOI: 10.1002/fld

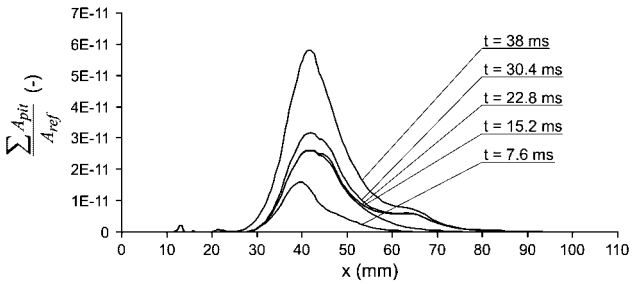

Figure 13. Time evolution of damage.

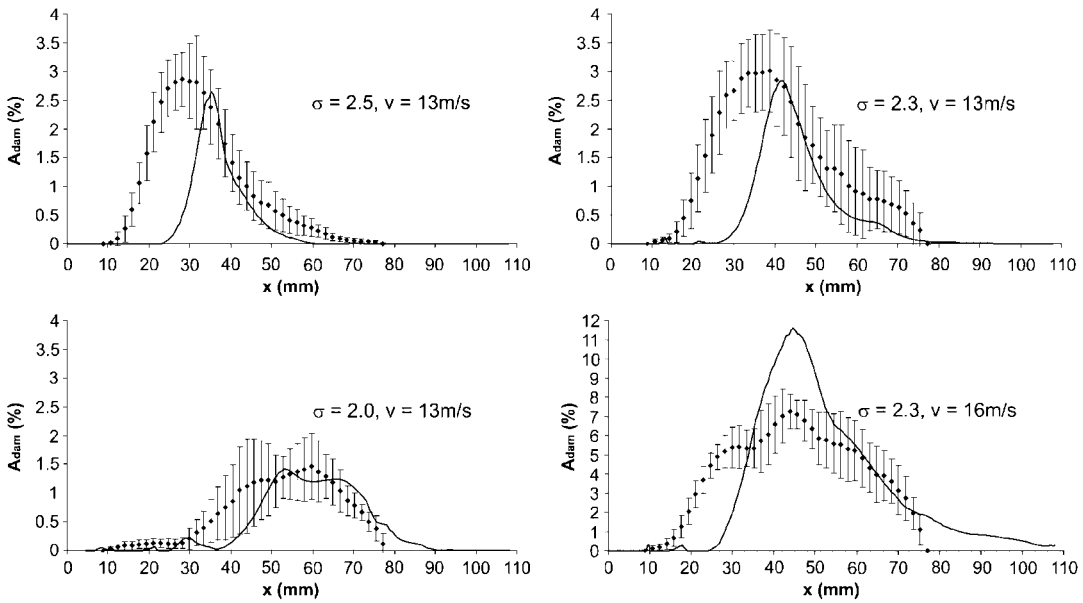

Figure 14. Measured and predicted damage on the surface.

even such a short simulation gives enough data for statistical averaging and extrapolation to a longer (experimentally observable) exposure to cavitation.

Numerical simulation of cavitation and consequently the prediction of cavitation erosion were performed in two dimensions only. On the other hand, erosion was measured over the whole surface of the hydrofoil. If one observes the pit diagrams in Figure 4, one can see that the pitting pattern over the span of the hydrofoil is far from uniform. Therefore, the experimental data are given as the value of damaged surface averaged over the span of the hydrofoil together with its standard deviation.

Diagrams in Figure 14 show the measured and numerically predicted damage on the hydrofoil after 1 h of exposure to cavitating flow, for tests 1–4.

DOI: 10.1002/fld

Table II. Predicted start of the mass loss.

	Cavitation number (dimensionless)	Velocity (m/s)	$t_{\text{mass loss}}$(h)
Test 1	2.0	13	164
Test 2	2.3	13	127
Test 3	2.5	13	172
Test 4	2.3	16	20

It can be observed that the numerical model relatively accurately predicts the magnitude and also the downstream extent of the damage. While the maximal damage magnitude is well predicted the upstream extent is not, especially for tests 2 and 3. It seems that the model concentrates the damage to a smaller region what is probably the result of the fluid dynamics simulation.

A classical discrepancy with the experiments in the CFD simulations of cavitating flows is the general aspect of the sheet cavity rear part. In the numerical results, the boundary of the two-phase flow area is very well delimited, whereas in reality the boundaries are 'soft' and the cavity wake is much fuzzier. Consequently, the pressure peaks are shorter in time (see Figure 11) and impact a smaller area in space. Also a shift between the measured and predicted damage can be seen. Since the shift is more or less constant (the predicted maximum occurs about 10 mm downstream of the measured one) this can be related to the uncertainty of setting of cavitation number and hydrofoil incidence angle.

In the case of higher velocity the model predicts much higher extent of the damage, which spreads also to the wedge part of the hydrofoil (measurements in this region were not performed).

In conclusion one can say that the model generally agrees with measurements in points like: the damage moves downstream as the cavitation number is decreased, at a constant velocity ($v=13\,\text{m/s}$) the most critical case lies at $\sigma=2.3$ and that the damage increases dramatically as the velocity is increased.

Finally, also the start of the mass loss can be predicted. This is done on the basis of recent work by the present author [27]. There cavitation erosion on a copper sample was observed during the incubation period and also mass loss was measured during long time exposure (several hundred hours) to the aggressive flow. It was found that the material starts to separate from the sample approximately at the time when in average 30% of the surface is covered by pits. Table II shows the predicted start of the mass loss process for the four investigated cases.

The predicted times cannot be directly compared with the experiment since measurements were performed only during the incubation period. Nevertheless the results seem plausible and are comparable to the results of investigations by Osterman *et al.* [27] if one takes into consideration that a somewhat less aggressive cavitation was observed during the present study. Apart from the case with higher flow velocity, the simulation predicts that the mass loss will first occur for the case of $\sigma=2.3$ and $v=13\,\text{m/s}$ although the time differences are not dramatic. The great influence of the flow velocity is again shown as the incubation period is predicted to end more than six times sooner for the case of high velocity than in the case of low flow velocity.

6. CONCLUSION

The present work is based on the coupling between several activities focusing on unsteady cavitating flows: (i) experimental investigations of cavitation erosion; (ii) PIV and high-frequency pressure

DOI: 10.1002/fld

measurements; (iii) numerical simulation of unsteady cavitating flow; and (iv) development of theoretical models for cavitation erosion. The final goal was to predict cavitation erosion by means of computational fluid dynamics (CFD) only. Although it is still impossible to imagine designing a new machine without any experimental verification, the newly developed erosion model and its coupling into a CFD code could significantly decrease the needed time and of the design process. Also when the predictions of long-term cavitation erosion are available in the early stage of the design more space for optimization of hydraulic shapes is available.

In previous paper [8], the same erosion model was used to predict erosion, but it was not coupled to a CFD simulation—there plausible results also on more complicated geometries such as a radial pump were achieved. Previous studies have also shown in various test cases, the capability of the CFD solver to detect as well the general behavior of unsteady cavitating behaviors including periodical vapor cloud shedding, as more subtle details of the two-phase flow structure.

In the present paper, a global model based on erosion and CFD simulations has been proposed to predict erosion cavitation on a 2D foil section. Experimental measurements of pressure and velocities close to the hydrofoil have also been used to validate the CFD results, while the damage measurements have been compared with the results of the proposed model.

Although this model is very simple, an interesting agreement between the predicted erosion and the experimental data was achieved. Intensity of erosion, as well as its downstream extent is generally correctly estimated. Conversely, significant disagreements have been found concerning the upstream limit of erosion. However, successful predictions of cavitation erosion by CFD methods depend strongly on the correct detection of the pressure wave intensity and duration. It suggests that the accuracy of the present results may be substantially increased if this point was improved: this may be obtained by applying other cavitation models leading to a better simulation of the sheet cavity rear part. This work is pursued currently in the LML laboratory.

ACKNOWLEDGEMENTS

Concerning the numerical part of this work, the authors would like to express their gratitude to the CNES (French Space Agency) for their continuous support. The cooperation between the institutions was supported by the Slovenia-France Cooperation in Science and Technology Program Proteus.

REFERENCES

1. Leighton TG. *The Acoustic Bubble*. Academic Press: London, 1997.
2. Benjamin TB, Ellis AT. The collapse of cavitation bubbles and the pressures thereby produced against solid boundaries. *Philosophical Transactions of the Royal Society of London* 1966; **260**:221–240.
3. Plesset MS, Chapman RB. Collapse of an initially spherical vapour cavity in the neighbourhood of a solid boundary. *Journal of Fluid Mechanics* 1971; **47**:283–290.
4. Lauterborn W, Bolle H. Experimental investigations of cavitation-bubble collapse in the neighbourhood of a solid boundary. *Journal of Fluid Mechanics* 1975; **72**:391–399.
5. Pereira F, Avellan F, Dupont Ph. Prediction of cavitation erosion: an energy approach. *Journal of Fluids Engineering* 1998; **120**:719–727.
6. Fortes-Patella R, Reboud JL, Briancon-Marjollet L. A phenomenological and numerical model for scaling the flow aggressiveness in cavitation erosion. *Workshop on Cavitation Erosion*, *Bassin d'essais des carènes*, Val de Reuil, France, 2004.
7. Dular M, Bachert B, Stoffel B, Sirok B. Relationship between cavitation structures and cavitation damage. *Wear* 2004; **257**:1176–1184.
8. Dular M, Stoffel B, Širok B. Development of a cavitation erosion model. *Wear* 2006; **261**(5–6):642–655.
9. Lush PA. Impact of a liquid mass on a perfectly plastic solid. *Journal of Fluid Mechanics* 1983; **135**:373–387.

DOI: 10.1002/fld

10. Dular M, Sirok B, Stoffel B. Influence of gas content in water and flow velocity on cavitation erosion aggressiveness. *Journal of Mechanical Engineering* 2005; **51**:132–145.
11. Dular M, Bachert R, Stoffel B, Sirok B. Experimental evaluation of numerical simulation of cavitating flow around hydrofoil. *European Journal of Mechanics—B/Fluids* 2005; **24**(4):522–538.
12. Dular M, Bachert R, Schaad C, Stoffel B. Investigation of a re-entrant jet reflection at an inclined cavity closure line. *European Journal of Mechanics—B/Fluids* 2007; **26**(5):688–705.
13. Böhm R. *Erfassung und hydrodynamische Beeinflussung fortgeschrittener Kavitationsustände und ihrer Aggressivität*. Technische Universität Darmstadt: Darmstadt, 1998.
14. Hofmann M. *Ein Beitrag zur Verminderung des erosiven Potentials kavitierender Stömungen*. Technische Universität Darmstadt: Darmstadt, 2001.
15. Fortes-Patella R, Reboud JL, Archer A. Cavitation damage measurement by 3D laser profilometry. *Wear* 2000; **246**:59–67.
16. Reboud JL, Fortes-Patella R, Archer A. Analysis of damaged surface. Part I. Cavitation mark measurements by 3D laser profilometry. *Proceedings of the 3rd ASME/JSME Joint Fluids Engineering Conference*, San Francisco, CA, 1999.
17. Dular M, Osterman A. Pit clustering in cavitation erosion. *Wear* 2008; **265**:811–820.
18. Knapp RT, Daily JT, Hammit FG. *Cavitation*. McGraw-Hill: New York, 1970.
19. Reboud J-L, Stutz B, Coutier O. Two phase flow structure of cavitation: experiment and modeling of unsteady effects. In *Proceedings of Third International Symposium on Cavitation*, Michel J-M, Kato H (ed.), Grenoble, France, 1998.
20. Coutier-Delgosha O, Reboud J-L, Delannoy Y. Numerical simulations in unsteady cavitating flows. *International Journal for Numerical Methods in Fluids* 2003; **42**:527–548.
21. Zhu J. A low diffusive and oscillation-free convection scheme. *Communications in Applied Numerical Methods* 1991; **7**:225.
22. Patankar SV. *Numerical Heat Transfer and Fluid Flow*. Hemisphere Publishing Corporation: Washington, DC, 1981.
23. Coutier-Delgosha O, Fortes-Patella R, Reboud J-L. Evaluation of the turbulence model influence on the numerical simulations of unsteady cavitation. *Journal of Fluids Engineering* 2003; **125**:38–45.
24. Coutier-Delgosha O, Fortes-Patella R, Reboud J-L. Simulation of unsteady cavitation with a two-equation turbulence model including compressibility effects. *Journal of Turbulence* 2002; **3**:058. Available from: http://jot.iop.org.
25. Wilcox D. *Turbulence Modeling for CFD*. DCW Industries, Inc.: La Canada, CA, U.S.A., 1998.
26. Orszag SA. *Renormalization Group Modelling and Turbulence Simulations*, *Near Wall Turbulent Flows*. Elsevier Science Publishers B.V.: Amsterdam, The Netherlands, 1993.
27. Osterman A, Bachert B, Sirok B, Dular M. Time dependant measurements of cavitation damage. *Wear* 2009; DOI: 10.1016/j.wear.2008.12.002.